# Three-Dimensional Modeling of Bipolar Charge-Carrier Transport and Recombination in Disordered Organic Semiconductor Devices at Low Voltages

Feilong Liu,[1] Harm van Eersel,[2] Peter A. Bobbert,[1,3] and Reinder Coehoorn[1,3,*]

[1] *Department of Applied Physics, Eindhoven University of Technology, P.O. Box 513, 5600 MB Eindhoven, Netherlands*

[2] *Simbeyond B.V., Groene Loper 5, 5612 AE Eindhoven, Netherlands*

[3] *Institute for Complex Molecular Systems, Eindhoven University of Technology, P.O. Box 513, 5600 MB Eindhoven, Netherlands*

(Received 28 July 2018; published 2 November 2018)

The electroluminescence from organic light-emitting diodes can be predicted with molecular-scale resolution using three-dimensional kinetic Monte Carlo (3D KMC) simulations [M. Mesta *et al.*, Nat. Mater. **12**, 652 (2013)]. However, around and below the built-in voltage KMC simulations are computationally inefficient. 3D master-equation (3D ME) simulation methods, which are fastest for low voltages, are so far mainly available for describing unipolar charge transport. In such simulations, the charge-carrier interactions are treated within a mean-field approach. It is not *a priori* evident whether such simulations, when applied to bipolar devices, can be extended to include the Coulomb attraction between the individual electrons and holes, so that charge-carrier recombination is sufficiently well described. In this work, we develop a systematic method for extending 3D ME simulations to bipolar devices. The method is applied to devices containing materials with Gaussian energetic disorder, and validated by a comparison with the results of 3D KMC simulations. The comparison shows that the 3D nonuniformity of the molecular-site-resolved carrier concentration and the one-dimensional layer-averaged profile of the recombination rate are fully retained, and that the 3D nonuniformity of the molecular-site-resolved recombination rate is fairly well retained.

DOI: 10.1103/PhysRevApplied.10.054007

## I. INTRODUCTION

In the past decades, tremendous progress has occurred in the field of disordered organic semiconductors. For example, organic light-emitting diodes (OLEDs), composed of layers of amorphous organic thin film, have already entered the display and lighting markets [1–7]. In order to understand the physics and speed up further device development, it is crucial to make use of device modeling techniques, which can both describe the essential physics and be computationally efficient.

For unipolar devices, various methods have been applied to disordered organic semiconductor devices, including one-dimensional drift-diffusion (1D DD) simulations, three-dimensional kinetic Monte Carlo (3D KMC) simulations, one-dimensional master-equation (1D ME) simulations, and three-dimensional master-equation (3D ME) simulations. 1D DD modeling is widely used for inorganic semiconductor devices. It has also been intensively used to model organic semiconductor devices [8–13], because the method is relatively simple and fast. However, the method has various limitations. For example, it assumes the system to be a continuous medium without explicitly including the details at the molecular level. These details are only implicitly included to a certain extent by making use of parameterized mobility functions that depend on the temperature $T$, carrier concentration $c$, and electric field $F$. The analytical expressions of the mobility function used are obtained from advanced 3D modeling methods [14–16]. Limitations of this approach include the proper treatment of charge-carrier relaxation effects [17–20] and the treatment of molecular-scale mixed materials such as those used in the emissive host-guest layers in OLEDs [21,22].

The limitations of 1D DD modeling can be overcome by 3D KMC modeling [23–30], first proposed by Bässler [17]. Assuming incoherent hopping of charge carriers between localized molecular states, 3D KMC modeling provides a mechanistic way to predict the macroscopic device characteristics from microscopic processes at the molecular level. This approach mimics, in a realistic manner, the functioning of devices by simulating the actual time and spatially resolved hopping motion of all charge carriers in a 3D system. The method is not constrained to specific layer structures, and has, e.g., been applied successfully to predictively simulate the electroluminescence in complex

*r.coehoorn@tue.nl

 

multilayer white OLEDs [27]. However, due to the inclusion of all microscopic-scale events, 3D KMC simulation can be computationally expensive and is under some conditions infeasible, especially when the device simulation is carried out around or below the built-in voltage $V_{bi}$, where the net device current density is due to only a very small imbalance of the diffusive motion of charge carriers in the positive and negative field directions. Moreover, in practice, 3D KMC simulations can also not be easily applied to simulate the transient device response as measured, e.g., using impedance spectroscopy.

Within master-equation methods, the time-averaged instead of the actual charge-carrier concentration on the molecular sites is calculated [31,32]. In contrast to 1D DD models, 1D ME methods [33] include, in a natural way, the discreteness of the molecular structure, also at internal interfaces. 3D ME modeling [14–16,28,32,34–38] can successfully bridge the gap between 1D DD and 3D KMC simulations. In 3D ME device simulations, the Coulomb interaction between a charge carrier and all other charges in the device is included in an approximate manner, viz. by using the layer-averaged instead of the actual space-charge density. Recently, we demonstrated the possibility to extend this approach by including the effects of the actual Coulomb interaction between the same types of charge carriers [39], which plays a role at large carrier concentrations and low electric fields. On the one hand, these 3D ME simulations of unipolar devices still include the effects of the energetically disordered 3D structure and the detailed intermolecular hopping-rate functions, if needed depending on the detailed distribution of relative orientations, distances, and transfer integrals between all molecules and based on a full-quantum approach that includes the effect of molecular reorganization by taking contributions from all vibrational modes into account [40]. On the other hand, the method is generally computationally less expensive than 3D KMC simulations, in particular below $V_{bi}$. This is shown in Fig. 1(a), which gives typical values for the simulation time required to obtain the current density at room temperature with a 1% accuracy, using 1D DD, 3D ME and 3D KMC simulations, for a 100-nm unipolar single-layer device. The lower and upper limits are obtained for materials with a very weak and strong Gaussian disorder (standard deviations $\sigma = 0.05$ and 0.12 eV), respectively. In addition to steady-state modeling, 3D ME simulations can also be used to predict transient properties of devices, such as those obtained using dark-injection [19] and impedance-spectroscopy measurements [20]. In these cases, 3D ME simulations are found to provide a much better agreement with experimental results than 1D DD simulations.

So far, the use of 3D ME modeling has almost exclusively been limited to unipolar devices. Extending unipolar 3D ME modeling to bipolar transport is not trivial. It is not *a priori* clear how in 3D ME simulations charge-carrier recombination and dissociation can be included in a manner that still allows predictive modeling of the device performance. Zhou *et al.* have proposed a 3D ME method

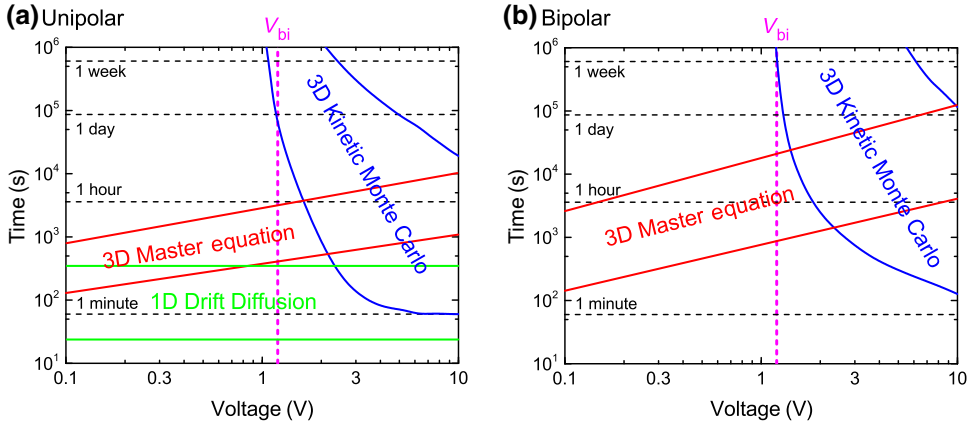


FIG. 1. Schematic pictures of the typical simulation time of three different models for 100-nm thick unipolar and bipolar disordered organic sandwich-type semiconductor devices of the type shown in Fig. 3(a). The 1D DD simulation employs the Bonham and Jarvis method [8], calculated with a Mathematica code [9] on a standard desktop computer. The 3D ME and 3D KMC simulations are performed on our local computer cluster at Eindhoven University of Technology. The 3D KMC simulation software used is Bumblebee, provided by Simbeyond B.V. (simbeyond.com) The 3D ME simulation method is presented in this paper. 1D DD simulation is computationally the most efficient, but it is not mechanistic. At voltages below $V_{bi}$, 3D ME modeling is the only feasible approach capable of 3D predictive modeling. We note that when carrying out the simulations for a device based on a semiconductor with a larger energy gap, but with identical injection barriers, essentially identical results will be obtained when expressed relative to the (larger) value of $V_{bi}$. We furthermore note that the simulation time shown here is obtained for normal numerical precision, and that for different hardware configurations, coding techniques, and device parameters, the actual simulation time may vary strongly. The readers are suggested to focus more on the general trends shown in this figure rather than the exact values of the simulation time.

within which recombination is treated as a *local* process, with a rate proportional to the product of the electron and hole concentration on the molecule at which the recombination takes place and with a phenomenological rate coefficient that is treated as a free parameter [41]. As shown in this paper, such an approach incorrectly neglects the consequences of the long-range nature of the Coulomb interaction between electrons and holes. Casalegno *et al.* have developed a 3D ME model that specifically focusses on organic solar cells [42]. A key challenge is then to properly describe the dissociation probability of charge-transfer (CT) excitons with the electron and hole residing on adjacent donor and acceptor sites, respectively. Within that model, the rate for this process and for the competing processes such as recombination are obtained from the results of KMC simulations of these processes for isolated CT excitons. A disadvantage of this approach is that such initial KMC simulations should be repeated when considering system or experimental variations, affecting, e.g., the material structure, energetic disorder, the binding energy of excitons localized on each molecule, dielectric constants, temperature, and local electric field.

In this paper, we develop a bipolar 3D ME model for the charge transport and recombination processes in sandwich-type devices based on disordered organic semiconductor materials such as OLEDs, with the aim to provide a computationally efficient method for predictive device modeling at low voltages. The model describes recombination as resulting from an interaction between an electron and a hole residing on nearest-neighbor sites, with a rate of the final recombination step that includes the effects of the percolative nature of the long-distance electron and hole transport towards each other. Without loss of computational efficiency, recombination is thus described effectively as a *nonlocal* process. We show how the effective rate coefficient can be obtained by comparing the results of KMC simulations with the results of a simple average-medium approach within which a mean-field approximation is used, and demonstrate the approach for the case of materials with a Gaussian density of states (DOS). The electron-hole recombination process is thus simulated without free parameters. Within the version of the model described in this paper, exciton formation is assumed to be followed by immediate radiative decay. However, the model is expected to provide a basis for efficient full 3D ME device models that also include exciton-transfer and exciton-loss processes. We find that the use of the 3D ME method developed in this paper enables efficient simulations at voltages below $V_{\mathrm{bi}}$. Fig. 1(b) gives the simulation time for a single-layer bipolar device with $V_{\mathrm{bi}} = 1.2$ V and shows a comparison with the time required for KMC simulations for the same device. We note that the same overall conclusions concerning the simulation time also hold for devices with larger values of $V_{\mathrm{bi}}$.

The structure of the paper is as follows. In Sec. II, the bipolar 3D ME model is formulated by describing the simulation approach and the method for deriving the recombination rate used in the model. In Sec. III, we apply the model to single-layer and realistic three-layer devices. The current density-voltage $J(V)$ characteristics, carrier-concentration profile and recombination profile are compared with the results of 3D KMC simulations, as well as the detailed site-resolved charge-carrier concentrations and recombination rates. Next, we compare the local versus the nearest-neighbor descriptions of recombination. Finally, we discuss, based on the simulations, the so-called ideality factor of bipolar devices, obtained from the simulated $J(V)$ curves below $V_{\mathrm{bi}}$. In the literature, measurements of the ideality factor have been used to deduce information about the nature of the recombination process [43,44]. Section IV contains a brief summary and an outlook.

## II. THE BIPOLAR 3D MASTER-EQUATION MODEL

### A. Simulation approach

In this section, the bipolar 3D ME model is formulated. As in unipolar 3D ME models for the charge transport in disordered organic semiconductors, we assume that the charge carriers occupy localized molecular states and that the charge transport is due to incoherent hopping between these states. The disordered organic semiconductor is described as a cubic lattice with a lattice constant $a$ (typically $a \sim 1$ nm), representing the actual molecular sites. All quantities referring to holes or electrons are denoted by superscripts $h$ and $e$, respectively. The DOS is assumed to be given by a Gaussian distribution with a width $\sigma$:

$$g(E) = \frac{1}{\sqrt{2\pi}\sigma} \exp\left(-\frac{E^2}{2\sigma^2}\right). \tag{1}$$

The charge-carrier hopping rate between neighboring sites, $\nu_{ij}$, is described by the Miller-Abrahams (MA) formula [45]:

$$\nu_{ij}^{h(e)} = \nu_1 \begin{cases} e^{-\Delta E_{ij}^{h(e)}/(k_B T)}, & \Delta E_{ij}^{h(e)} > 0, \\ 1, & \Delta E_{ij}^{h(e)} \leqslant 0. \end{cases} \tag{2}$$

Here $\nu_1$ is the hopping attempt rate to a first nearest neighbor (at a distance $a$), $k_B$ is the Boltzmann constant, $\Delta E_{ij}$ is the energy difference between sites $j$ and $i$, and $T$ is the temperature. We note that recent theoretical work has indicated that for amorphous organic semiconductors the MA formula provides often a quite accurate description of vibrational-mode effects on the hopping rate, and that a description of the charge transport, as obtained using MA theory, is often more accurate than a description obtained

using the semiclassical Marcus theory [46]. For simplicity, we assume in this paper that the molecular wave functions decay rapidly in space so that the charge carriers can only hop between nearest-neighbor sites [47]. The hopping rates are deduced using the self-consistently calculated site-energy differences $\Delta E_{ij}$ that include the intrinsic energy difference due to Gaussian disorder and the electrostatic potential difference between sites $i$ and $j$, as obtained by solving the 1D Poisson equation. In this approach, the Coulomb interaction with the space charge, averaged over each molecular layer, is thus taken into account, but the three-dimensional character of the actual Coulomb interaction between a charge and all other individual charges is neglected [24,39]. When providing a comparison with the results from KMC simulations, we focus on systems within which Coulomb-correlation effects between carriers of the same polarity are very weak. The effect of the Coulomb attraction between carriers of opposite polarity, leading to recombination, is described in a manner as discussed below.

The time evolution of the hole and electron occupation probability (concentration) on site $i$, $c_i$, is determined by the hopping of holes or electrons from all neighboring sites $j$ toward site $i$ and vice versa (as in unipolar models [14–16,28,32,34–38]), minus a contribution due to exciton formation:

$$\frac{dc_i^h}{dt} = \sum_j \left[ \begin{array}{l} \nu_{ji}^h c_j^h (1-c_i^h) - \nu_{ij}^h c_i^h (1-c_j^h) \\ -\gamma(\tilde{\nu}_{ji}^e + \tilde{\nu}_{ij}^h)(c_i^h c_j^e - c_{i0}^h c_{j0}^e) \end{array} \right], \tag{3a}$$

$$\frac{dc_i^e}{dt} = \sum_j \left[ \begin{array}{l} \nu_{ji}^e c_j^e (1-c_i^e) - \nu_{ij}^e c_i^e (1-c_j^e) \\ -\gamma(\tilde{\nu}_{ji}^h + \tilde{\nu}_{ij}^e)(c_i^e c_j^h - c_{i0}^e c_{j0}^h) \end{array} \right]. \tag{3b}$$

The coefficients $\gamma$ and the rates $\tilde{\nu}$ are defined and further discussed below. The exciton formation process is described as a special type of hopping process. When a hole is located on site $i$ and an electron is located on a neighboring site $j$, an exciton formation event can occur and an exciton may be formed on either site $i$ or $j$. The general structure of the exciton formation term is that of the Langevin recombination rate formula: the formation rate is proportional to the product of the electron and hole occupation probabilities on the two sites [48–52]. At equilibrium, detailed balance is preserved by the thermal generation term $c_{i0}c_{j0}$, in which $c_{i0}$ and $c_{j0}$ are the equilibrium hole and electron concentrations at site $i$ and $j$, respectively. The electron and hole concentrations at equilibrium are calculated self-consistently by solving the 1D Poisson equation combined with Fermi-Dirac statistics. In this paper, we assume that the excitons formed by electron-hole recombination decay immediately to the ground state. Excitonic interaction processes (such as exciton diffusion, exciton-exciton annihilation, exciton-polaron quenching, etc.) are thus not included. We intend to include such interactions in future work.

From the Langevin expression, the exciton formation rate is expected to be proportional to the sum of the electron and hole mobilities [48–52]. The exciton generation term is, therefore, taken to be proportional to the sum of the local electron and hole hop rates, modified by taking into account that upon exciton formation these rates are affected by the exciton binding energy, $E_{\mathrm{exc},b}$,

$$\tilde{\nu}_{ij}^{h(e)} = \nu_1 \begin{cases} e^{-\Delta\tilde{E}_{ij}^{h(e)}/(k_B T)}, & \Delta\tilde{E}_{ij}^{h(e)} > 0, \\ 1, & \Delta\tilde{E}_{ij}^{h(e)} \leqslant 0, \end{cases} \tag{4}$$

with

$$\Delta\tilde{E}_{ij}^{h(e)} = \Delta E_{ij}^{h(e)} - E_{\mathrm{exc},b}. \tag{5}$$

For disordered small-molecule organic semiconductors, $E_{\mathrm{exc},b}$ can be as large as 1 eV, or more [53,54]. $E_{\mathrm{exc},b}$ depends on the exciton spin (singlet, triplet). For notational simplicity, we have omitted this dependence in Eq. (5). From the Langevin expression, it follows that the exciton formation rate prefactor $\gamma$ is proportional to $\varepsilon_r\varepsilon_0/e$, with $\varepsilon_r$ the dielectric constant, $\varepsilon_0$ vacuum permittivity, and $e$ the elementary charge. The prefactor should furthermore take into account that for disordered materials the mobility that would follow within a mean-field approach from the average of the hopping rates between nearest-neighbor sites, employed in Eq. (2), is much larger than the actual value. In Sec. II B, we develop an analytical expression for $\gamma$. The set of coupled equations given by Eq. (2) is solved iteratively. When carrying out device simulations, the image charge effect on carrier injection is taken into account in the same way as in Ref. [33]. The metal electrodes are modeled as additional layers of sites, ensuring both charge injection and extraction. The total current density is $J = J^h + J^e$, with

$$J^h = \frac{e}{L_x L_y L_z} \sum_{i,j} \left\{ \left[ \nu_{ij}^h c_i^h (1-c_j^h) + \gamma \tilde{\nu}_{ij}^h (c_i^h c_j^e - c_{i0}^h c_{j0}^e) \right] (x_j - x_i) \right\}, \tag{6a}$$

and

$$J^e = -\frac{e}{L_x L_y L_z} \sum_{i,j} \left\{ \left[ \nu_{ij}^e c_i^e (1-c_j^e) + \gamma \tilde{\nu}_{ij}^e (c_i^e c_j^h - c_{i0}^e c_{j0}^h) \right] (x_j - x_i) \right\}, \tag{6b}$$

with $L_x$, $L_y$, and $L_z$ the device dimensions in the electric-field direction and the two lateral directions, respectively, and $(x_j - x_i)$ the distance between sites $i$ and $j$ in the direction of the electric field. In the two lateral directions, periodic boundary conditions are used. The recombination

rate per unit volume on site $i$ is given by

$$R_i = \frac{\gamma}{a^3}\sum_j \left[\tilde{\nu}^e_{ji}(c^h_i c^e_j - c^h_{i0}c^e_{j0}) + \tilde{\nu}^h_{ji}(c^e_i c^h_j - c^e_{i0}c^h_{j0})\right], \quad (7)$$

where the summation is over all nearest-neighbor sites.

### B. Recombination rate prefactor $\gamma$

In this subsection, we derive a theoretical expression for the recombination rate prefactor $\gamma$ that enters Eq. (3). Consistent with the results of KMC simulations [55], we require that in systems with spatially uniform and equal electron and hole concentrations, $c^h = c^e = c$, the recombination rate at low electric fields and for disorder energies $\sigma > 0.05$ eV is, to a good approximation, given by the Langevin formula. For the cases $c^h \neq c^e$, the theoretical derivation is less straightforward. However, it will be shown in Sec. III that for realistic device simulations, in which $c^h \neq c^e$ is common, the derived $\gamma$ in this section also works rather well. The Langevin formula can be written as

$$R_{\mathrm{KMC}} = \frac{e}{\varepsilon_r\varepsilon_0} 2\mu_{\mathrm{bip}}(c)\frac{c^2}{a^6}, \quad (8)$$

where $\mu_{\mathrm{bip}}(c) \equiv r_\mu(c)\mu(c)$ is the so-called bipolar mobility. The analysis thus takes into account that in bipolar systems the electron-hole Coulomb interaction leads to mobilities that are slightly enhanced, by a factor $r_\mu$, as compared to the unipolar values [55]. When expressing the effective (site-occupation-weighted) difference between the rates of the final recombination step with and without the effects of the exciton binding energy in terms of a factor $r_\nu$, a comparision with Eq. (8) yields

$$\gamma = \frac{e}{a^3\varepsilon_r\varepsilon_0} r_\mu r_\nu \frac{2\mu c^2}{\langle\sum_j (\nu^e_{ji}c^h_i c^e_j + \nu^h_{ji}c^e_i c^h_j)\rangle_i}. \quad (9)$$

For notational simplicity, the dependence of $\gamma$, $\mu$, $r_\mu$, and $r_\nu$ on $c$ is not explicitly shown.

In the absence of energetic disorder, the occupation probabilities are at all sites equal to $c$, and the unipolar mobility is (for small fields) given by $\mu = a^2\nu_1 e/(k_B T)$. Furthermore, $r_\nu = 1$, because all final hops leading to recombination are barrierless, even when $E_{\mathrm{exc},b} = 0$. From Eq. (9), the recombination prefactor is then

$$\gamma = \frac{e^2}{3\varepsilon_r\varepsilon_0 a k_B T} r_\mu \quad \text{(no disorder)}. \quad (10)$$

For materials with Gaussian disorder, the relationship between the unipolar mobility and the nearest-neighbor hop rates is less straightforward. The unipolar mobility is from the extended Gaussian disorder model (EGDM) given by [14,56]

$$\mu(c) \cong \frac{a^2 e\nu_1}{\sigma} \times f\,(\hat{\sigma}, c)_{\mathrm{EGDM}} \times \exp\left[-0.42\hat{\sigma}^2\right], \quad (11)$$

with $f\,(\hat{\sigma}, c)_{\mathrm{EGDM}}$ the carrier-concentration enhancement of the mobility with respect to the mobility for small concentrations, in the independent-particle Boltzmann regime, and with $\hat{\sigma} \equiv \sigma/(k_B T)$. The exponential factor expresses the temperature dependence of the mobility in the low-concentration limit, and includes the effects of the percolative motion of the charge carriers in the disordered material. In contrast, the denominator in Eq. (9) does not include the effects of percolation, and therefore overestimates the rate with which electron-hole encounter processes will occur. The mobility that would follow from such a weighted summation of local hopping rates, termed the mean medium approximation (MMA) [57–60], is for the case of nearest-neigbour hopping in a Gaussian DOS given by (see Sec. SI of the Supplemental Material [61])

$$\mu(c) \cong \frac{2\beta a^2 e\nu_1}{\sigma} f\,(\hat{\sigma}, c)_{\mathrm{MMA}} \exp\left[-0.25\hat{\sigma}^2\right], \quad (12)$$

with $\beta = 0.562$ and $f\,(\hat{\sigma}, c)_{\mathrm{MMA}}$ a function that in the limit of strong disorder becomes equal to the charge-carrier-concentration enhancement of the mobility with respect to the mobility for small carrier concentrations (see Figs. S1 and S2 of the Supplemental Material [61]). For small disorder parameters, $f\,(\hat{\sigma}, c)_{\mathrm{MMA}}$ approaches $\hat{\sigma}/2\beta$, consistent with the expression for the mobility in the disorderless limit, given above. Based on these results, we include the effect of percolation in the expression for the recombination prefactor by generalizing Eq. (10) in the following manner:

$$\begin{aligned}\gamma &= \frac{e^2 r_\mu r_\nu}{3\varepsilon_r\varepsilon_0 a k_B T}\frac{\mu_{\mathrm{EGDM}}}{\mu_{\mathrm{MMA}}} \\ &= \frac{e^2 r_\mu r_\nu}{6\beta\varepsilon_r\varepsilon_0 a k_B T}\frac{f_{\mathrm{EGDM}}}{f_{\mathrm{MMA}}}\exp\left[-0.17\,\hat{\sigma}^2\right]. \end{aligned} \quad (13)$$

This theoretical approach is expected to yield a useful parameterization scheme describing the disorder, temperature, and carrier-concentration dependence of the value of $\gamma$ that leads to optimal agreement between 3D ME and 3D KMC results. Based on Eq. (13), we write

$$\gamma \cong A_{\mathrm{th}}\frac{e^2}{\varepsilon_r\varepsilon_0 a k_B T}\exp\left[-B_{\mathrm{th}}\hat{\sigma}^2\right], \quad (14)$$

with, from the theory developed above, $A_{\mathrm{th}} = r_\mu r_\nu f_{\mathrm{EGDM}}/(6\beta f_{\mathrm{MMA}})$ and $B_{\mathrm{th}} \cong 0.17$. Both parameters are dimensionless.

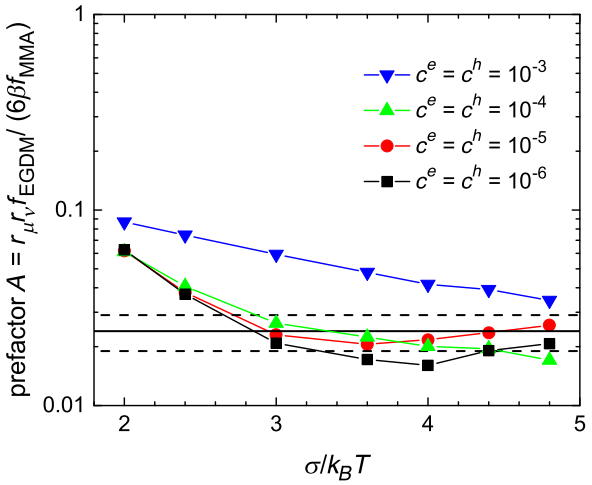


FIG. 2. Calculated prefactor, $A = r_\mu r_\nu f_{EGDM}/(6\beta f_{MMA})$, as a function of disorder parameter $\hat{\sigma} = \sigma/k_BT$ and carrier concentration $c$. The full horizontal line at $A = 0.024$ gives the optimized value for which the simulations presented in Sec. III are carried out, and the dashed horizontal lines at $A = 0.019$ and 0.029 indicate the uncertainty range, based on the simulation results for a large number of devices studied in Sec. II of the Supplemental Material. For calculational details, see Sec. SI of the Supplemental Material [61].

In Fig. 2, the value of $A_{th}$ as a function of the disorder parameter $\hat{\sigma}$ and the carrier concentration $c$ is given (details of the evaluation are given in Fig. S3 of the Supplemental Material [61]). Surprisingly, although $f_{EGDM}$, $f_{MMA}$, $r_\mu$, and $r_\nu$ are all $\hat{\sigma}$ and $c$ dependent, their combination $A_{th}$ is only weakly sensitive to $\hat{\sigma}$ and $c$ in the range $3 \leq \hat{\sigma} \leq 5$ and $10^{-6} \leq c \leq 10^{-4}$. In Fig. S3, it is shown that both $f_{EGDM}$ and $f_{MMA}$ increase with $\hat{\sigma}$ and $c$, and in the expression of $A$, they approximately cancel each other. Furthermore, $r_\mu$ increases with $\hat{\sigma}$ and $c$, while $r_\nu$ decreases with $\hat{\sigma}$ and $c$. Hence, their product in the expression of $A$ also becomes almost $\hat{\sigma}$ and $c$ independent, except for the case of $c = 10^{-3}$. In Sec. III, we show from a comparison of 3D ME and 3D KMC simulation results for a large number of devices with varying material parameters and layer thicknesses, studied for a wide application-relevant voltage and temperature range, that a satisfactory agreement is obtained when simply using a constant value $A = 0.024 \pm 0.005$, combined with $B \cong 0.154$. This finding significantly reduces the computational cost in 3D ME modeling, because instead of updating $\gamma$ for all molecular sites during each iteration step, it is, to a good approximation, allowed to use a single value for the entire device.

In realistic devices, it is possible that the DOS of the HOMO and LUMO have different widths, i.e., $\sigma^e \neq \sigma^h$. In this case, by benchmarking the 3D ME results with 3D KMC, we find that using an effective $\sigma_{eff} = \min(\sigma^e, \sigma^h)$ in Eq. (14) yields a good agreement. We view this as a result of the different roles of the two carriers: the carriers on molecules with the larger $\sigma$ will be trapped and the recombination is most likely due to capture of the more mobile other type of carrier, on molecules with a smaller $\sigma$. Examples of device simulations with unequal $\sigma^e$ and $\sigma^h$ can be found in Fig. S4 (devices 5, 6, and 7) of the Supplemental Material [61].

## III. 3D BIPOLAR DEVICE SIMULATIONS

In this section, the results of device simulations using the bipolar 3D ME model are compared with the results of 3D KMC simulation results. We also show simulation results for $V < V_{bi}$, where only the 3D ME model can be used. The simulations are carried out using a constant recombination prefactor $\gamma$, of the form given by Eq. (14), and with the optimized parameters $A = 0.024$ and $B = 0.154$, as explained in the previous section.

### A. Current density-voltage characteristics and profiles of the charge-carrier concentration, recombination rate, and electric field

As an example, we study 100-nm-thick devices, with the layer structure shown in Fig. 3(a).

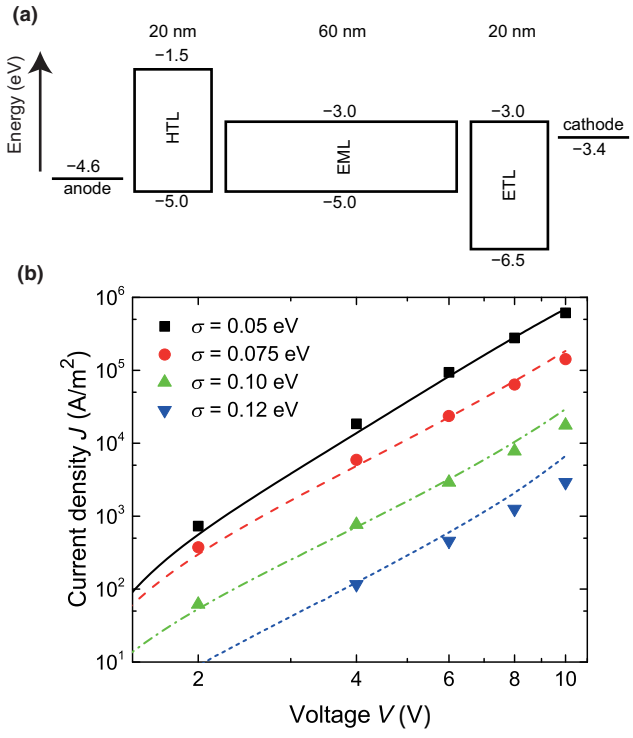


FIG. 3. (a) Band diagram of an example bipolar symmetric three-layer device. (b) Current density-voltage characteristics calculated from 3D ME (curves) and 3D KMC (symbols) for different energetic disorder energies $\sigma$. $T = 290$ K.

We assume a lattice constant $a = 1$ nm, hopping attempt frequency $\nu_1 = 3.3 \times 10^{10}$ s$^{-1}$, relative dielectric constant $\varepsilon_r = 3$, and temperature $T = 290$ K. The HOMO and LUMO energies are assumed to be uncorrelated. We choose a relatively large injection barrier (0.4 eV) in order to suppress the unipolar Coulomb correlation effect [39]. This effect can, in principle, be included, but this is outside the scope of this paper. For simplicity we take $\sigma^e = \sigma^h = \sigma$. The simulations typically include 10 disorder configurations to obtain sufficient statistics. The lateral dimensions of the devices simulated are typically $50 \times 50$ nm$^2$. In realistic devices (e.g., OLEDs), a three-layer structure is commonly used, consisting of a hole transport layer (HTL), an emissive layer (EML), and an electron transport layer (ETL). In Fig. 3(a), the schematic band diagram for a simple symmetric three-layer HTL(20 nm)/EML(60 nm)/ETL(20 nm) device is shown. In Fig. 3(b), the simulated current density-voltage characteristics of this device for different energetic disorder $\sigma$ is plotted. The agreement between the ME and KMC results is very good for low and moderate voltages. Deviations are observed for large voltages at large disorder.

In Fig. 4, the electron and hole concentration profile, the recombination profile, and the electric field profile are shown for the device shown in Fig. 3(a) with $\sigma = 0.10$ eV. The agreement between the 3D ME and 3D KMC simulations is very good at low voltages ($V = 2$ and 4 V). At large voltages ($V = 10$ V), the 3DME simulations do not reproduce the 3D KMC results well. We suspect that this is because our model for recombination [Eqs. (8)–(14)] is based on the low electric-field regime, which cannot be directly applied to high electric fields (i.e., $eVa/L \sim \sigma$). Such high electric fields add complexity to the recombination process [55]. The 3D ME model in this case underestimates the local recombination rate, leading to an overestimation of the carrier concentration and current density [62,63]. This is consistent with the current density-voltage simulation results in Fig. 3. We note that at these large voltages 3D KMC simulations are computationally as efficient or even more efficient than 3D ME simulations. Therefore, we have not extended the 3D ME model to include high-field cases.

To further validate the 3D bipolar ME model, we compare, in Sec. SII of the Supplemental Material[61], the current density-voltage characteristics, charge-carrier profile, and recombination profile of 3D ME and 3D KMC simulations for 32 additional devices. The following device parameters are varied (Table SI of the Supplemental Material [61]): width of the energetic disorder ($\sigma = 0.05$, 0.075, 0.10, or 0.12 eV), disorder energies for HOMO and LUMO ($\sigma^e \neq \sigma^h$, for the combination of 0.05/0.075 eV, 0.05/0.10 eV, or 0.075/0.10 eV), disorder energies $\sigma$ in different layers (HTL/EML/ETL $\sigma = 0.05/0.10/0.05$ eV or 0.10/0.05/0.10 eV), hopping attempt frequency of electrons and holes ($\nu_1^e \neq \nu_1^h$, e.g., $\nu_1^h = 10\nu_1^e$ in HTL and EML), hopping attempt frequency $\nu_1$ in different layers ($\nu_1^e$ and $\nu_1^h$ in HTL and ETL are 10, 100, or 1000 times larger than those in EML), device thicknesses or layer thicknesses $L$ (HTL/EML/ETL thickness = 10/30/10, 5/90/5, 10/80/10, 30/40/30, or 40/20/40 nm), temperature ($T =$

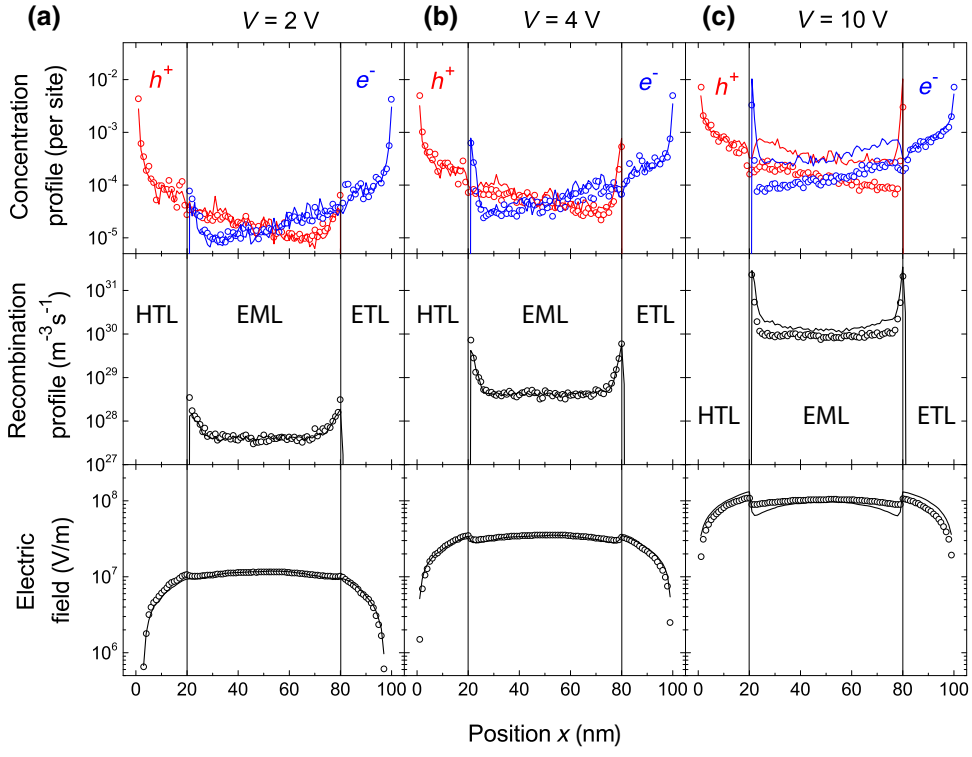


FIG. 4. Time-averaged electron and hole concentration profile (top), recombination profile (middle), and electric field profile (bottom) at different voltages for the device shown in Fig. 3(a), with $\sigma = 0.10$ eV. Curves, 3D ME results. Symbols, 3D KMC results.

250, 320, or 387 K), injection barrier ($\Phi = 0.2$, 0.3, 0.5, or 0.6 eV), and dielectric constant ($\varepsilon_r = 4$ or 6). At low voltages ($V \leq 4$ V), the 3D ME simulation results agree in most cases well with the results from 3D KMC simulations (Fig. S4 of the Supplemental Material [61]). There exist a few cases where deviations in the carrier-concentration profiles are observed. However, in these cases the agreement in the current density-voltage characteristics and the recombination profile (which are more important for device characteristics) is still good. In addition to model validation, these simulation data sets also provide physical insight into device optimization. For example, a possible approach to obtain a uniform emission profile in the EML is to set the disorder energy $\sigma$ in the EML to be larger than those in ETL and HTL (see, e.g., device 32 in Fig. S4 of the Supplemental Material [61]).

### B. Site-resolved charge-carrier concentrations and recombination rates

In Sec. III A, the 3D ME and 3D KMC charge-carrier and recombination profiles are compared in a layer-averaged way. However, due to the energetic disorder, the charge-carrier occupation probability and the recombination rate associated with each molecular site are highly inhomogeneous. A more strict test of the 3D ME model is to compare the site-resolved concentration and recombination rates with the 3D KMC results. In Fig. 5, such a comparison is shown for the device in Fig. 3(a) with $\sigma = 0.10$ eV, at $V = 3$ V. The disorder configurations are taken to be the same for the ME and KMC simulations. In the figure, the molecular sites are labeled with a site number by descending order of

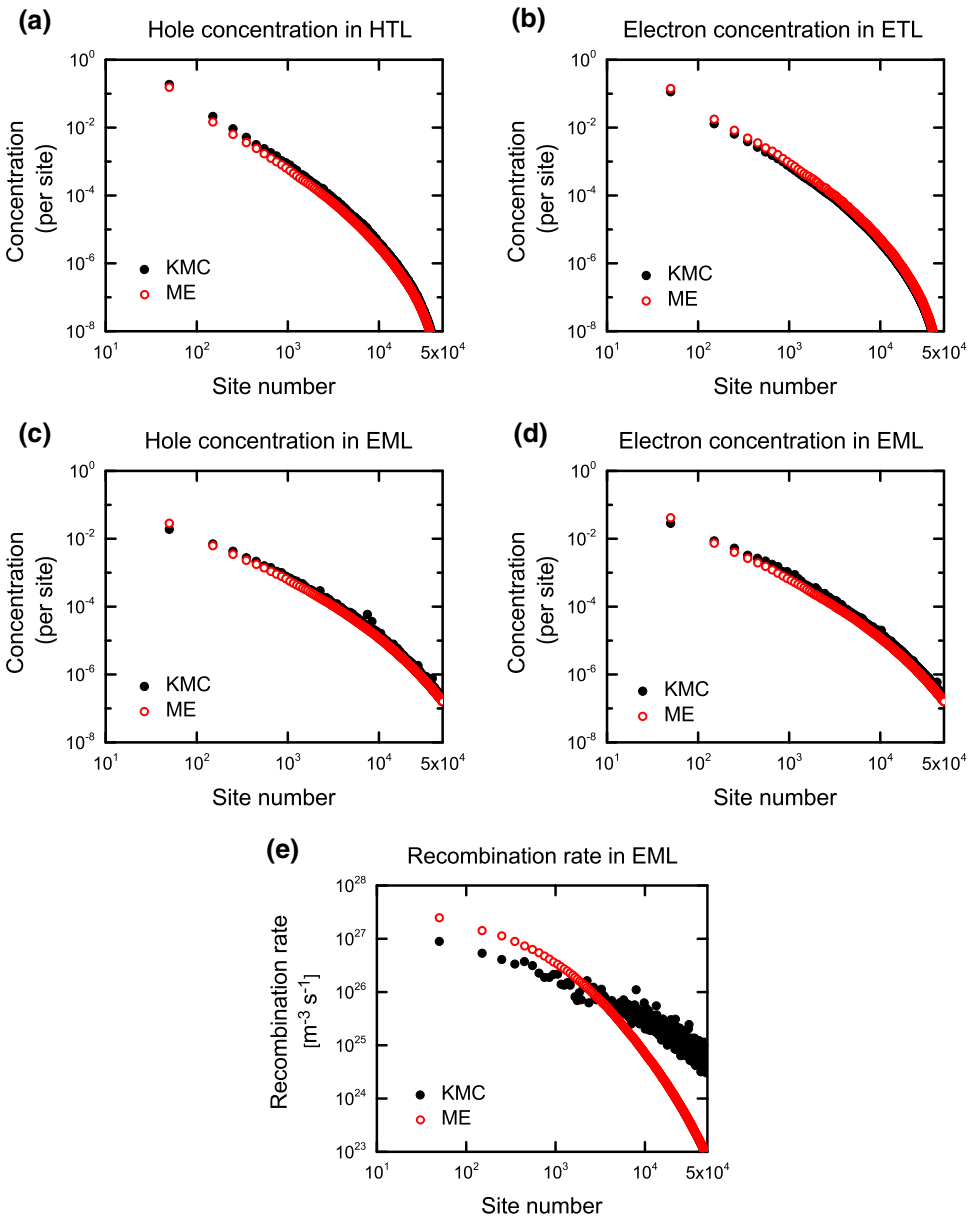


FIG. 5. Correlation of molecular-site-resolved charge-carrier concentrations and recombination rates as obtained from 3D ME and 3D KMC simulations, for the device shown in Fig. 3(a) with $\sigma = 0.10$ eV, at $V = 3$ V. The results are binned in groups of 100 sites. (a) Hole concentration in the HTL. (b) Electron concentration in the ETL. (c) Hole concentration in the EML. (d) Electron concentration in the EML. (e) Recombination rate in the EML. The ETL/HTL in the simulations contains $20 \times 50 \times 50 = 5 \times 10^4$ molecular sites. The EML in the simulations contains $60 \times 50 \times 50 = 1.5 \times 10^5$ molecular sites. The sites with very low carrier concentrations or recombination rates are not shown due to statistical insufficiency in the simulations.

carrier concentration (or recombination rate), as calculated from the 3D ME simulations. The same site numbers are assigned to the KMC simulation results. The KMC-calculated and ME-calculated site-resolved concentrations or rates are both shown as a function of the site number. To obtain better statistics, the results are binned for every 100 sites.

The results in Fig. 5 show that the site-resolved electron and hole concentrations calculated using the 3D ME simulations can very well reproduce those calculated from the 3D KMC simulations. The site-resolved recombination rates as obtained from the 3D ME and 3D KMC simulations are excellently correlated. However, for sites at which the recombination rates from 3D KMC simulations is relatively large, the 3D ME simulations overestimate the recombination rate by a factor 2–3. As the recombination rate is largest in thin zones near the EML/HTL and EML/ETL interfaces, we view this overestimation as a consequence of neglecting the carrier concentration gradients in these regions on a 2–5 nm scale. The

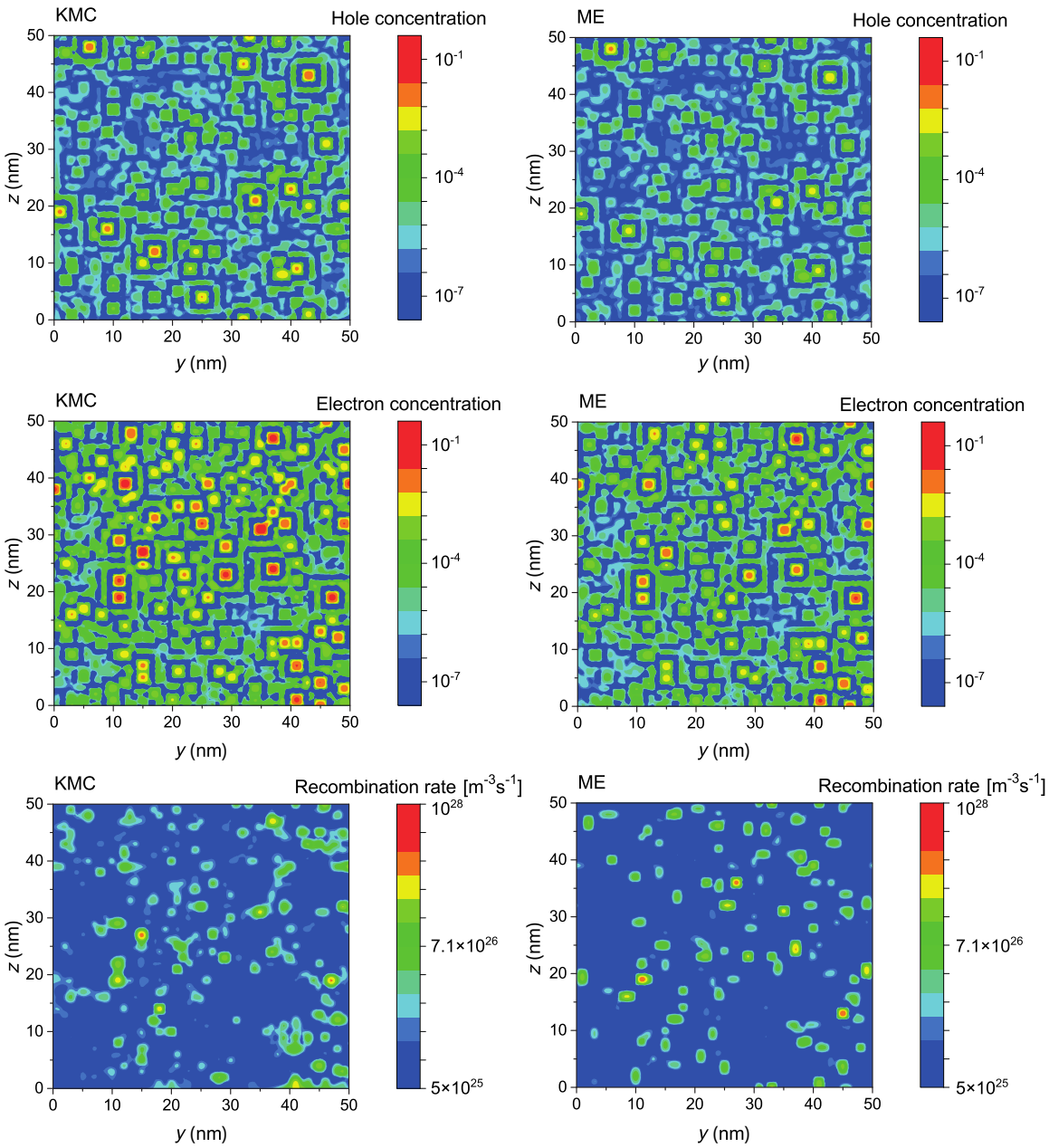


FIG. 6. 2D cross-sectional plots of the molecular site-resolved hole (top) and electron (middle) concentration profiles and recombination rate profiles (bottom) in the layer at $x = 21$ nm (the layer in the EML that is adjacent to the EML/HTL interface) for the device shown in Fig. 3(a) at $V = 3$ V. The red (blue) color regions denote a high (low) carrier concentration or recombination rate in the device. Left panels, 3D KMC simulation results. Right panels, 3D ME simulation results.

recombination rate on sites at which in the 3D KMC simulation recombinations seldomly take place is underestimated by the 3D ME simulations.

To better visualize the site-resolved results, we show in Fig. 6 cross sections of the device in Fig. 3 and plot the 2D contour profile of carrier concentration and recombination rate. The hot spots correspond to sites with high carrier concentrations or recombination rates. Consistent with Fig. 5, while the site-resolved carrier concentration in KMC is well reproduced by ME, the site-resolved recombination rate shows some differences.

### C. Local versus nearest-neighbor descriptions of recombination

In Eq. (4), recombination has been described as a nearest-neighbor process, instead of a local process with a rate at site $i$ proportional to $c_i^h c_i^e$, as in Ref. [41]. In order to compare the effect of these two alternative approaches, we compare the results of 3D ME and 3D KMC simulations for a 100-nm single-layer device with a symmetric energy level structure as shown in the inset of Fig. 7 for the case of positive, negative, and vanishing correlation between the HOMO and LUMO energies (see the top part of Fig. 7). As was shown in Ref. [38], both types of disorder can be found in actual materials: electrostatic fields give rise to a positive correlation and configurational disorder can give rise to negative correlation. A robust model should be valid for all cases. Fig. 7 shows that KMC simulations reveal that the type of correlation has no significant effect on the device current density. This is because the main driving force for the last step of recombination is the exciton binding energy, which is much larger than the energetic disorder $\sigma$. This result is well reproduced by the percolation-corrected nearest-neigbour ME model proposed in this paper (full curves in the figure). In contrast, using a local ME model, as in Ref. [41], would give rise to strongly deviating results (dashed curves).

### D. Current-voltage characteristics below the built-in voltage

To further investigate the validity of the bipolar 3D ME simulation model, we examine the current density-voltage characteristics around and below the built-in voltage $V_{\rm bi}$. In this regime, the current density is dominated by diffusion rather than drift. The current increases exponentially with voltage. KMC simulations are then not realistically applicable due to an impractically long simulation time (Fig. 1). In this subsection, we study the dependence of the ideality factor $\eta$, which is defined as $\eta = [k_B T/e \cdot d(\ln J)/dV]^{-1}$, on the disorder energy, voltage, and temperature. The 3D ME simulation results are shown in Figs. 8 and 9.

The ideality factor, obtained from the slope of the current density-voltage characteristics, enters the generalized Einstein relation between the diffusivity $D$ and the mobility

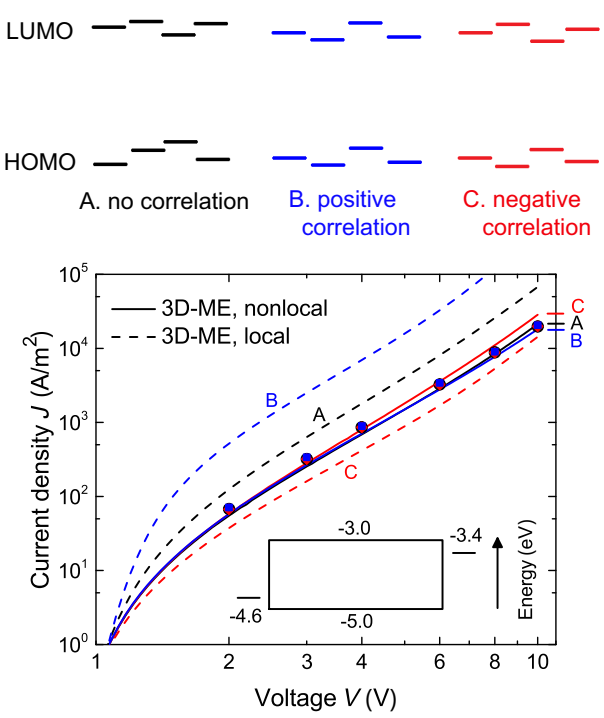


FIG. 7. Calculated current density-voltage characteristics for a symmetric bipolar single-layer device, with uncorrelated, correlated, or anticorrelated HOMO-LUMO energy levels. Symbols, 3D KMC simulation. Solid curves, 3D ME simulation with a mechanistic nonlocal recombination description, proposed in this paper. Dashed curves, ME simulation with a local recombination description [41]. The parameters are as follows: $\sigma = 0.10$ eV, $T = 290$ K, device thickness $L = 100$ nm. The rate prefactor is $\nu_1 = 3.3 \times 10^{10}$ s$^{-1}$, which is also used as the rate prefactor in the local recombination model. The energy level diagram is shown schematically in the inset of the figure.

$\mu$, $D = \eta \mu k_B T/e$ [9,43,44,50,59]. For nondegenerate inorganic semiconductors, $\eta = 1$. For disordered organic semiconductors, with a Gaussian DOS, $\eta > 1$ when the DOS is filled above the critical concentration beyond which the system is no longer in the independent-particle (Boltzmann) regime. The ideality factor $\eta$ is a function of the disorder parameter $\hat{\sigma}$ and the carrier concentration $c$ (see Tables SII and SIII of the Supplemental Material [61]). In a device, the carrier-concentration profile is not uniform (see Figs. S6 and S8 of the Supplemental Material [61]), which implies that the ideality factor as deduced from experiments can depend on the voltage at which it has been determined, as shown below.

It is not straightforward to directly compare the simulated ideality factor with the experimentally measured ideality factor in the literature [43,44,50]. The difference might be due to three reasons. (a) In our simulations we consider a Gaussian DOS, but in reality there might be a superimposed exponential trap DOS, which is not included in our model. The exponential trap DOS will

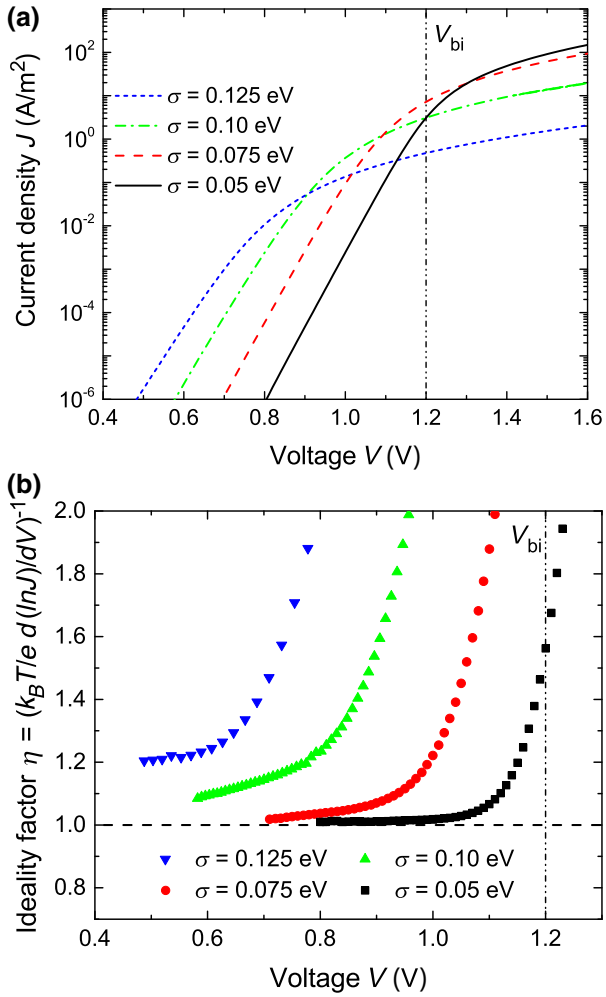


FIG. 8. (a) Current density-voltage characteristics at low voltages (diffusion-dominated region) for different disorder energies $\sigma$ at temperature $T = 290$ K. (b) Corresponding ideality factor as a function of voltage. The results are calculated from 3D ME simulations. The device structure is shown in Fig. 3(a).

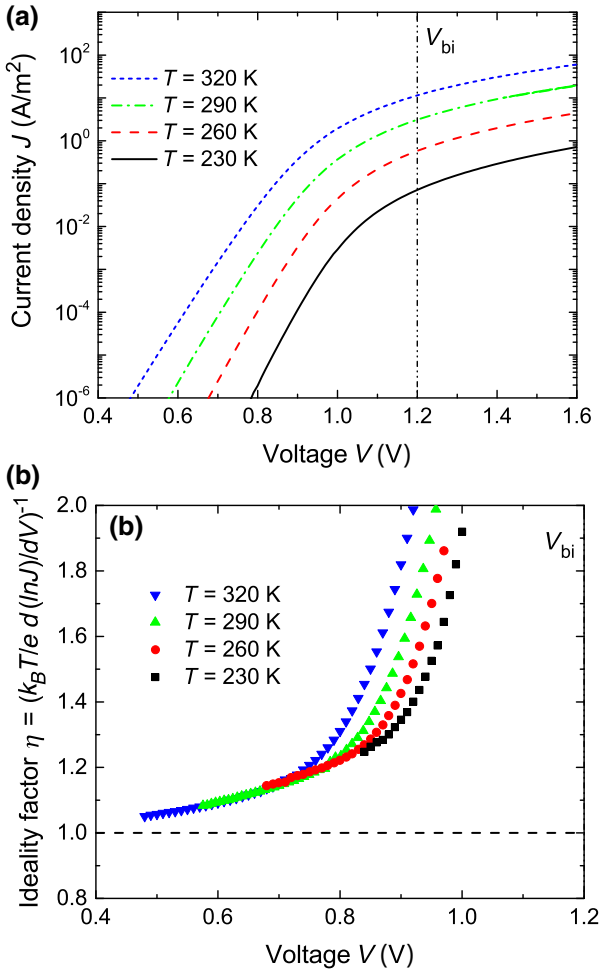


FIG. 9. (a) Current density-voltage characteristics at low voltages (diffusion-dominated region) for different temperatures $T$ at disorder energy $\sigma = 0.10$ eV. (b) Corresponding ideality factor as a function of voltage. The results are calculated from 3D ME simulations. The device structure is shown in Fig. 3(a).

significantly modify the ideality factor. (b) As the ideality factor is extracted from the slope of the current density-voltage characteristics, the choice of voltage point affects the extracted ideality factor (see above). (c) In reality, there is usually a leakage current in the low-voltage regime, which is not included in the simulation. The leakage current is expected to influence the ideality factor. Hence, one needs to be careful regarding the physical interpretation of the ideality factor.

In Fig. 8, the disorder energy $\sigma$ is varied while the temperature $T$ is fixed at 290 K. Fig. 8(a) shows that for large $\sigma$ and low voltages, the current density is larger than that for the small $\sigma$ case. This is, at least in part, due to the easier injection from the electrodes into a wider DOS. Fig. 8(b) shows that the ideality factor is indeed voltage dependent. For small $\sigma$ and low voltages, the ideality factor approaches unity. In the voltage range studied, it increases with $\sigma$. This effect can be explained from the increasing charge-carrier concentration, at any point in the device, with increasing $\sigma$, combined with the increase with $\sigma$ of the diffusion coefficient enhancement factor at any given carrier concentration [9,43,59].

In Fig. 9, the disorder energy $\sigma$ is fixed at 0.10 eV while the temperature $T$ is varied. We observe that the ideality factor is almost independent of temperature, which agrees with experimental results [44]. We also find that for a series of symmetric 100-nm devices with varying EML layer thicknesses the ideality factor, evaluated at a fixed low voltage, is not significantly dependent on the voltage (see Sec. SIII of the Supplemental Material [61]). We remark that accurate calculation of the ideality factor requires high precision in the current density-voltage calculation. To run the 3D ME simulations with a sufficiently high precision for a current density as low as $10^{-6}$ A/m$^2$,

the simulation time is significantly larger than those shown in Fig. 1.

## IV. CONCLUSIONS AND OUTLOOK

In this paper, we present a bipolar 3D ME simulation model that can be used to predictively model electron-hole recombination in disordered organic semiconductor devices at low voltages. For voltages close to or smaller than the built-in voltage $V_{bi}$, the simulation method is numerically much more efficient than 3D KMC simulations. The model is validated by comparing the simulation results for a wide range of parameters with those obtained from 3D KMC simulations. From the development of a theoretical expression for the recombination prefactor $\gamma$ (Eq. (13)), we gain deepened understanding of the factors that determine the recombination rate in disordered organic semiconductors.

The bipolar 3D ME model presented in this work opens up a route towards strongly accelerated OLED device simulations. It can be further extended and improved in various ways. In this work, the simulations are limited to organic semiconductors with a Gaussian DOS. It is important in the future to extend the model beyond a Gaussian DOS, because in practice (a) the emissive layers are composed of a host-guest system [4–6], and (b) in some materials an exponential DOS of traps is present [27,64]. We envisage that the methodology for including recombination, developed in Sec. II B for the case of a Gaussian DOS and based on a comparison of percolation and mean-field-based transport theories, can be extended to other types of density of states. No calibration using KMC simulations would then be needed. It is also important to extend the model to include excitonics (e.g., exciton diffusion, recombination, annihilation, quenching, intersystem crossing, etc. [4–6,21,22,27]), which is crucial for OLED simulations. However, while in 3D KMC simulations these processes could be added straightforwardly, in 3D ME simulations the inclusion of these processes requires deeper insight into the device physics.

## ACKNOWLEDGMENTS

This work is part of the research program "3D Master Equation simulations for Next-Generation OLEDs (MENGO)" with Project No. 16KIEMH01, which is jointly financed by the Netherlands Organization for Scientific Research (NWO) and Simbeyond B.V. This research is also part of the Dutch-German project "Modeling of organic light-emitting diodes: From molecule to device" (MODEOLED), funded on the Dutch side by the Dutch Technology Foundation (STW; Project No. 12200), which is part of the Dutch Science Foundation (NWO), and on the German side by the "Deutsche Forschungsgemeinschaft" (DFG; Project No. WE1863/22-1).

[1] C. W. Tang and S. A. VanSlyke, Organic electroluminescent diodes, Appl. Phys. Lett. **51**, 913 (1987).
[2] W. Brütting, J. Frischeisen, T. D. Schmidt, B. J. Scholz, and C. Mayr, Device efficiency of organic light-emitting diodes: Progress by improved light outcoupling, Phys. Status Solidi A **210**, 44 (2013).
[3] J. H. Burroughes, D. D. C. Bradley, A. R. Brown, R. N. Marks, K. Mackay, R. H. Friend, P. L. Burns, and A. B. Holmes, Light-emitting diodes based on conjugated polymers, Nature **347**, 539 (1990).
[4] M. A. Baldo, D. F. O'Brien, Y. You, A. Shoustikov, S. Sibley, M. E. Thompson, and S. R. Forrest, Highly efficient phosphorescent emission from organic electroluminescent devices, Nature **395**, 151 (1998).
[5] H. Uoyama, K. Goushi, K. Shizu, H. Nomura, and C. Adachi, Highly efficient organic light-emitting diodes from delayed fluorescence, Nature **492**, 234 (2012).
[6] S. Hirata, Y. Sakai, K. Masui, H. Tanaka, S. Y. Lee, H. Nomura, N. Nakamura, M. Yasumatsu, H. Nakanotani, Q. Zhang, K. Shizu, H. Miyazaki, and C. Adachi, Highly efficient blue electroluminescence based on thermally activated delayed fluorescence, Nat. Mater. **14**, 330 (2015).
[7] B. Geffroy, P. le Roy, and C. Prat, Organic light-emitting diode (OLED) technology: Materials, devices and display technologies, Polym. Int. **55**, 572 (2006).
[8] J. S. Bonham and D. H. Jarvis, Theory of space-charge-limited current with one blocking electrode, Aust. J. Chem. **31**, 2103 (1978).
[9] S. L. M. van Mensfoort and R. Coehoorn, Effect of Gaussian disorder on the voltage dependence of the current density in sandwich-type devices based on organic semiconductors, Phys. Rev. B **78**, 085207 (2008).
[10] P. S. Davids, I. H. Campbell, and D. L. Smith, Device model for single carrier organic diodes, J. Appl. Phys. **82**, 6319 (1997).
[11] B. K. Crone, P. S. Davids, I. H. Campbell, and D. L. Smith, Device model investigation of bilayer organic light emitting diodes, J. Appl. Phys. **87**, 1974 (2000).
[12] F. Liu, P. P. Ruden, I. H. Campbell, and D. L. Smith, Device model for electronic processes at organic/organic interfaces, J. Appl. Phys. **111**, 094507 (2012).
[13] E. Knapp, R. Häusermann, H. U. Schwarzenbach, and B. Ruhstaller, Numerical simulation of charge transport in disordered organic semiconductor devices, J. Appl. Phys. **108**, 054504 (2010).
[14] W. F. Pasveer, J. Cottaar, C. Tanase, R. Coehoorn, P. A. Bobbert, P. W. M. Blom, D. M. de Leeuw, and M. A. J. Michels, Unified Description of Charge-Carrier Mobilities in Disordered Semiconducting Polymers, Phys. Rev. Lett. **94**, 206601 (2005).
[15] M. Bouhassoune, S. L. M. van Mensfoort, P. A. Bobbert, and R. Coehoorn, Carrier-density and field-dependent charge-carrier mobility in organic semiconductors with correlated Gaussian disorder, Org. Electron. **10**, 437 (2009).
[16] A. Massé, P. Friederich, F. Symalla, F. Liu, R. Nitsche, R. Coehoorn, W. Wenzel, and P. A. Bobbert, Ab initio

charge-carrier mobility model for amorphous molecular semiconductors, Phys. Rev. B **93**, 195209 (2016).
[17] H. Bässler, Charge transport in disordered organic photoconductors a Monte Carlo simulation study, Phys. Stat. Sol. (b) **175**, 15 (1993).
[18] A. Melianas, F. Etzold, T. J. Savenije, F. Laquai, O. Inganäs, and M. Kemerink, Photo-generated carriers lose energy during extraction from polymer-fullerene solar cells, Nat. Commun. **6**, 8778 (2015).
[19] M. Mesta, C. Schaefer, J. de Groot, J. Cottaar, R. Coehoorn, and P. A. Bobbert, Charge-carrier relaxation in disordered organic semiconductors studied by dark injection: Experiment and modeling, Phys. Rev. B **88**, 174204 (2013).
[20] M. Mesta, J. Cottaar, R. Coehoorn, and P. A. Bobbert, Study of charge-carrier relaxation in a disordered organic semiconductor by simulating impedance spectroscopy, Appl. Phys. Lett. **104**, 213301 (2014).
[21] L. Zhang, H. van Eersel, P. A. Bobbert, and R. Coehoorn, Clarifying the mechanism of triplet-triplet annihilation in phosphorescent organic host-guest systems: A combined experimental and simulation study, Chem. Phys. Lett. **652**, 142 (2016).
[22] R. Coehoorn, L. Zhang, P. A. Bobbert, and H. van Eersel, Effect of polaron diffusion on exciton-polaron quenching in disordered organic semiconductors, Phys. Rev. B **95**, 134202 (2017).
[23] J. Zhou, Y. C. Zhou, J. M. Zhao, C. Q. Wu, X. M. Ding, and X. Y. Hou, Carrier density dependence of mobility in organic solids: A Monte Carlo simulation, Phys. Rev. B **75**, 153201 (2007).
[24] J. J. M. van der Holst, F. W. A. van Oost, R. Coehoorn, and P. A. Bobbert, Monte Carlo study of charge transport in organic sandwich-type single-carrier devices: Effect of Coulomb interactions, Phys. Rev. B **83**, 085206 (2011).
[25] I. A. Howard, F. Etzold, F. Laquai, and M. Kemerink, Nonequilibrium charge dynamics in organic solar cells, Adv. Energy Mater. **4**, 1301743 (2014).
[26] N. J. van der Kaap and L. J. A. Koster, Massively parallel kinetic Monte Carlo simulations of charge carrier transport in organic semiconductors, J. Comp. Phys. **307**, 321 (2016).
[27] M. Mesta, M. Carvelli, R. J. de Vries, H. van Eersel, J. J. M. van der Holst, M. Schober, M. Furno, B. Lüssem, K. Leo, P. Loebl, R. Coehoorn, and P. A. Bobbert, Molecular-scale simulation of electroluminescence in a multilayer white organic light-emitting diode, Nat. Mater. **12**, 652 (2013).
[28] P. Kordt, J. J. M. van der Holst, M. A. Helwi, W. Kowalsky, F. May, A. Badinski, C. Lennartz, and D. Andrienko, Modeling of organic light emitting diodes: From molecular to device properties, Adv. Funct. Mater. **25**, 1955 (2015).
[29] M. C. Heiber, C. Baumbach, V. Dyakonov, and C. Deibel, Encounter-Limited Charge-Carrier Recombination in Phase-Separated Organic Semiconductor Blends, Phys. Rev. Lett. **114**, 136602 (2015).
[30] H. Li, Y. Li, H. Li, and J.-L. Brédas, Organic field-effect transistors: A 3D kinetic Monte Carlo simulation of the current characteristics in micrometer-sized devices, Adv. Funct. Mater. **27**, 1605715 (2017).
[31] Z. G. Yu, D. L. Smith, A. Saxena, R. L. Martin, and A. R. Bishop, Molecular Geometry Fluctuation Model for the Mobility of Conjugated Polymers, Phys. Rev. Lett. **84**, 721 (2000).
[32] Z. G. Yu, D. L. Smith, A. Saxena, R. L. Martin, and A. R. Bishop, Molecular geometry fluctuations and field-dependent mobility in conjugated polymers, Phys. Rev. B **63**, 085202 (2001).
[33] R. Coehoorn and S. L. M. van Mensfoort, Effects of disorder on the current density and recombination profile in organic light-emitting diodes, Phys. Rev. B **80**, 085302 (2009).
[34] J. A. Freire and G. Voss, Master equation approach to charge injection and transport in organic insulators, J. Chem. Phys. **122**, 124705 (2005).
[35] J. J. M. van der Holst, M. A. Uijttewaal, B. Ramachandhran, R. Coehoorn, P. A. Bobbert, G. A. de Wijs, and R. A. de Groot, Modeling and analysis of the three-dimensional current density in sandwich-type single-carrier devices of disordered organic semiconductors, Phys. Rev. B **79**, 085203 (2009).
[36] N. Tessler, Y. Preezant, N. Rappaport, and Y. Roichman, Charge transport in disordered organic materials and its relevance to thin-film devices: A tutorial review, Adv. Mater. **21**, 2741 (2009).
[37] F. Liu, A. Massé, P. Friederich, F. Symalla, R. Nitsche, W. Wenzel, R. Coehoorn, and P. A. Bobbert, Ab initio modeling of steady-state and time-dependent charge transport in hole-only $\alpha$-NPD devices, Appl. Phys. Lett. **109**, 243301 (2016).
[38] A. Massé, P. Friederich, F. Symalla, F. Liu, V. Meded, R. Coehoorn, W. Wenzel, and P. A. Bobbert, Effects of energy correlations and superexchange on charge transport and exciton formation in amorphous molecular semiconductors: An ab initio study, Phys. Rev. B **95**, 115204 (2017).
[39] F. Liu, H. van Eersel, B. Xu, J. G. E. Wilbers, M. P. de Jong, W. G. van der Wiel, P. A. Bobbert, and R. Coehoorn, Effect of Coulomb correlation on charge transport in disordered organic semiconductors, Phys. Rev. B. **96**, 205203 (2017).
[40] X. de Vries, P. Friederich, W. Wenzel, R. Coehoorn, and P. A. Bobbert, Full quantum treatment of charge dynamics in amorphous molecular semiconductors, Phys. Rev. B **97**, 075203 (2018).
[41] W. Zhou, C. Zimmermann, and C. Jungemann, *2015 International Conference on Simulation of Semiconductor Processes and Devices (SISPAD)* (IEEE Electron Devices Society, Piscataway, NJ, USA, 2015), p. 136.
[42] M. Casalegno, A. Bernardi, and G. Raos, Numerical simulation of photocurrent generation in bilayer organic solar cells: Comparison of master equation and kinetic Monte Carlo approaches, J. Chem. Phys. **139**, 024706 (2013).
[43] G. A. H. Wetzelaer, L. J. A. Koster, and P. W. M. Blom, Validity of the Einstein Relation in Disordered Organic Semiconductors, Phys. Rev. Lett. **107**, 066605 (2011).
[44] K. Harada, A. G. Werner, M. Pfeiffer, C. J. Bloom, C. M. Elliott, and K. Leo, Organic Homojunction Diodes with a High Built-in Potential: Interpretation of the Current-Voltage Characteristics by a Generalized Einstein Relation, Phys. Rev. Lett. **94**, 036601 (2005).
[45] A. Miller and E. Abrahams, Impurity conduction at low concentrations, Phys. Rev. **120**, 745 (1960).
[46] X. de Vries, P. Friederich, W. Wenzel, R. Coehoorn, and P. A. Bobbert, Full quantum treatment of charge dynamics in amorphous molecular semiconductors, Phys. Rev. B **97**, 075203 (2018).

[47] We note that within a more refined approach, the distance ($d$) dependence of the hopping rate is given by an additional factor $\exp[-2d/\lambda]$, with a wavefunction decay length $\lambda$ that is typically in the range 0.1–0.3 nm [17,65,66].

[48] L. J. A. Koster, V. D. Mihailetchi, and P. W. M. Blom, Bimolecular recombination in polymer/fullerene bulk heterojunction solar cells, Appl. Phys. Lett. **88**, 052104 (2006).

[49] U. Albrecht and H. Bässler, Langevin-type charge carrier recombination in a disordered hopping system, Phys. Stat. Sol. (b) **191**, 455 (1995).

[50] M. Kuik, L. J. A. Koster, G. A. H. Wetzelaer, and P. W. M. Blom, Trap-Assisted Recombination in Disordered Organic Semiconductors, Phys. Rev. Lett. **107**, 256805 (2011).

[51] F. Liu, P. P. Ruden, I. H. Campbell, and D. L. Smith, Exciplex current mechanism for ambipolar bilayer organic light emitting diodes, Appl. Phys. Lett. **99**, 123301 (2011).

[52] T. M. Burke, S. Sweetnam, K. Vandewal, and M. D. McGehee, Beyond Langevin recombination: How equilibrium between free carriers and charge transfer states determines the open-circuit voltage of organic solar cells, Adv. Energy Mater. **5**, 1500123 (2015).

[53] M. Knupfer, Exciton binding energies in organic semiconductors, Appl. Phys. A **77**, 623 (2003).

[54] H. Yoshida and K. Yoshizaki, Electron affinities of organic materials used for organic light-emitting diodes: A low-energy inverse photoemission study, Org. Electron. **20**, 24 (2015).

[55] J. J. M. van der Holst, F. W. A. van Oost, R. Coehoorn, and P. A. Bobbert, Electron-hole recombination in disordered organic semiconductors: Validity of the Langevin formula, Phys. Rev. B **80**, 235202 (2009).

[56] R. Coehoorn, W. F. Pasveer, P. A. Bobbert, and M. A. J. Michels, Charge-carrier concentration dependence of the hopping mobility in organic materials with Gaussian disorder, Phys. Rev. B **72**, 155206 (2005).

[57] V. Rodin, F. Symalla, V. Meded, P. Friederich, D. Danilov, A. Poschlad, G. Nelles, F. von Wrochem, and W. Wenzel, Generalized effective-medium model for the carrier mobility in amorphous organic semiconductors, Phys. Rev. B **91**, 155203 (2015).

[58] Y. Roichman and N. Tessler, Charge transport in conjugated polymers – The influence of charge concentration, Synth. Met. **135–136**, 443 (2003).

[59] Y. Roichman, Y. Preezant, and N. Tessler, Analysis and modeling of organic devices, Phys. Stat. Sol. (a) **201**, 1246 (2004).

[60] I. I. Fishchuk, A. K. Kadashchuk, J. Genoe, M. Ullah, H. Sitter, Th. B. Singh, N. S. Sariciftci, and H. Bässler, Temperature dependence of the charge carrier mobility in disordered organic semiconductors at large carrier concentrations, Phys. Rev. B **81**, 045202 (2010).

[61] See Supplemental Material at http://link.aps.org/supplemental/10.1103/PhysRevApplied.10.054007 for detailed derivation of $\gamma$ in Sec. II B, systematic benchmarking of the bipolar 3D ME model with the 3D KMC model over a wide device parameter range, cross section of molecular-site-resolved charge-carrier concentration and recombination rate contour plots, and more discussions on the ideality factor.

[62] R. H. Parmenter and W. Ruppel, Two-carrier space-charge-limited current in a trap-free insulator, J. Appl. Phys. **30**, 1548 (1959).

[63] H. C. F. Martens, W. F. Pasveer, H. B. Brom, J. N. Huiberts, and P. W. M. Blom, Crossover from space-charge-limited to recombination-limited transport in polymer light-emitting diodes, Phys. Rev. B **63**, 125328 (2001).

[64] F. May, B. Baumeier, C. Lennartz, and D. Andrienko, Can Lattice Models Predict the Density of States of Amorphous Organic Semiconductors? Phys. Rev. Lett. **109**, 136401 (2012).

[65] O. Rubel, S. D. Baranovskii, and P. Thomas, Concentration dependence of the hopping mobility in disordered organic solids, Phys. Rev. B **69**, 014206 (2004).

[66] H. van Eersel, P. A. Bobbert, R. A. J. Janssen, and R. Coehoorn, Monte Carlo study of efficiency roll-off of phosphorescent organic light-emitting diodes: Evidence for dominant role of triplet-polaron quenching, Appl. Phys. Lett. **105**, 143303 (2014).